Multi-Drive Road Map Generation on Standardized High-Velocity Roads using Low-Cost Sensor Data

Maximilian Naumann* and André-Marcel Hellmund*

FZI Research Center for Information Technology
Mobile Perception Systems
76131 Karlsruhe, Germany
{naumann,hellmund}@fzi.de

Abstract—Highly accurate digital road maps are the status quo for advanced driver assistance systems and automated driving functions. To achieve high map accuracies, recent approaches deployed high-cost and high-precision sensor systems. This paper proposes a novel automated map generation framework for standardized high-velocity roads using a low-cost sensor system composed of a monocular camera and a low-precision GNSS receiver. To compensate for the lower precision, the map is generated from multiple measurement drives.

The map is subdivided into a global base line, describing the road course, and a grid containing lane marking information. The integration of a new measurement drive is performed by separate updates of the base line and the grid. To increase the accuracy of the input data, GNSS measurements are fused with vehicle motion data obtained from a new approach to visual odometry on highly standardized roads, the Lane Marking Based Visual Odometry (LMBVO).

Evaluation results on a German highway emphasize the advantages of the partitioned map representation. The global map accuracy is in the range of meters, while a high accuracy in the centimeter range is achieved for the local grid, so that the generated maps are suitable for automated driving functions on high-velocity roads.

Fig. 1. **Overview of Multi-Drive Map Generation Framework.**

I. INTRODUCTION

Current advanced driver assistance systems as well as recent research studies on highly automated driving require detailed knowledge and comprehension of the local environment to handle the complexity and variety of today's traffic scenarios [1]. Therefore, highly accurate digital maps are the status quo to enhance online sensor data with offline computed supplemental information on the road network. The information stored in the map ranges from high-level topological data like the number of available lanes down to low-level data like precise road courses or the locations and types of road markings [2].

The requirements imposed on the deployed digital maps are three-fold. Firstly, the map data must be time-accurate containing the latest reconstructions of the road network. Secondly, large areas of the network must be covered. And thirdly, the accuracy of metric data must fulfill the specifications of respective driving functions. The map accuracy for automated driving is demanded to be in the low decimeter range [3].

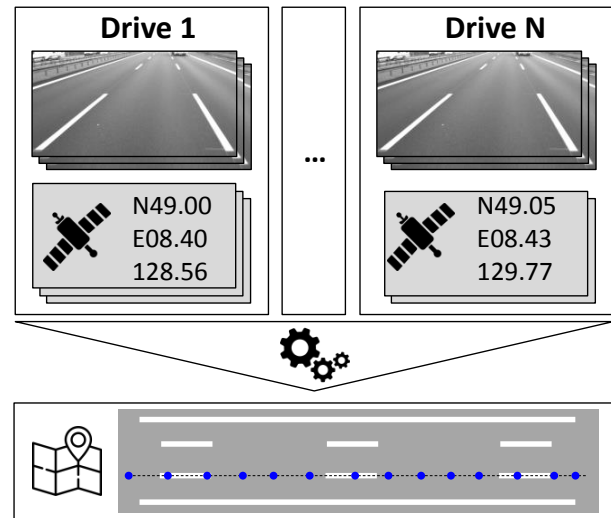Current approaches mostly use high-cost measurement vehicles, equipped with LIDAR, RTK-DGPS and high-resolution stereo or surround view camera systems to generate the digital road maps [4], [5], [6], [7]. While those approaches easily achieve the desired map accuracy, providing up-to-date map data for large areas with a high coverage of available landmarks is an expensive and time consuming effort. More recent studies [8], [9] consequently set the focus on low-cost sensor data. The advantage of using low-cost sensor data is that a multitude of *inexpensive* probe vehicles may be used to map large road network areas redundantly. The main disadvantage is that low-cost sensors are typically less accurate.

In this paper, we present a novel approach to the automated map generation on standardized, high-velocity roads, such as the German Autobahn, utilizing a low-cost monocular camera and a low-precision GNSS receiver to accurately represent lane markings of road carriageways. The map generation is performed in a multi-drive setup to compensate for the lower precision and to address the landmark existence problem, meaning that individual lane markings may be obscured in single drives.

Core components of the overall map generation framework

*The authors contributed equally.

(Figure 1) are the single-drive processing, the map representation and the map fusion. In single-drive processing, lane markings are extracted from the recorded image sequence and mapped into a global reference coordinate system. In order to improve the position accuracy, we introduce a simple but promising visual odometry algorithm for low-structured, standardized road environments.

The map representation is split into two parts, a base line describing the road course in *global* coordinates and a *local* grid, storing the lane marking data relative to the base line. The advantages of this separation are twofold. Firstly, the global and local parts may be updated independently using different features for the fusion. Secondly, this representation inherently supports different map accuracies, having a high local accuracy while only providing a moderate global accuracy.

The map fusion incorporates a new drive into the existing map by fusing the base lines and grids.

The algorithms presented in this work are currently subject to some restrictions and limitations. The carriageways to be mapped have to be free of construction works and the lane markings are assumed to be static, i.e. they do not change in-between drives. Furthermore, highway intersections interconnecting two highway carriageways are currently not considered, but will be included in future work.

The remainder of this paper is organized as follows. Section II reviews the related work. Section III introduces the map generation framework, whereof the newly proposed visual odometry algorithm is described in depth in section IV. The proposed algorithms are finally evaluated in section V.

II. RELATED WORK

Recent publications related to the automated generation of road maps can be divided into three groups depending on the deployed sensor devices: aerial images, pure GNSS traces and the combination of image and GNSS data.

In [10], an approach is introduced to generate road maps from aerial images. The drawback of this approach is the landmark coverage problem due to streets being partly or fully obscured by cars, buildings, clouds or flora at the time of recording. Additionally, up-to-date aerial imagery data is hardly available for low cost.

The second group of map generation techniques purely uses massive GNSS traces, e.g. from commodity GNSS receivers, to automatically deduce information about drivable lanes and corridors [11], [12]. While the semantic road information is easily deducible from those traces, detailed landmarks, e.g. for precise lateral localization, are not available. Furthermore, the derived lane positions are subject to systematic errors [4].

The third category of approaches mostly resembles the sensor setup chosen in this work using combined GNSS and image data as input. Former approaches used highly accurate DGPS sensors [4], [5], [6], [7], as subsumed in [9].

More recently, *Guo et al.*[8] proposed an algorithm using standard GNSS, INS and visual odometry data, resulting in noticeably better vehicle positioning than loosely coupled GNSS/INS integration approaches. The global map is divided into fixed local segments, based on a basic map. Afterwards, top-view images are accumulated along the position tracks for each segment. The lane graph is subsequently constructed by approximating a clothoid spline through the lane center lines.

Schreiber et al. [9] developed an automated multi-drive map generation algorithm for GNSS and stereo image input data. The generation is split into single-drive processing for each drive and a succeeding multi-drive processing. The association between individual drives is based on variations in dashed lane marking sequences. Finally, vehicle poses and lane markings are optimized in a SLAM-like manner using non-linear least square optimization.

III. MAP GENERATION CONCEPT

This section introduces the fundamental building blocks of the automated map generation framework. The nomenclature for this section is depicted in figure 2 showing the carriageway on a standardized road. The layout of the road is assumed to be regulated with regard to curvatures[1], lane widths and lane markings. Lane markings are expected to have fixed widths and to be either solid or dashed. Dashed lane markings have predefined, fixed dash and gap lengths. As another prerequisite, the uncertainty of GNSS measurements of the low-cost receiver is assumed to lie in the meter range [13].
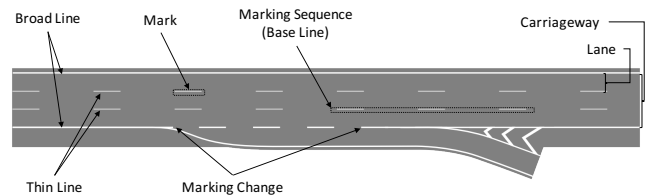

Fig. 2. **Lane Marking Nomenclature.**

The framework is divided into 5 steps as outlined in figure 3. Each measurement drive is processed individually and fused with the current map, hereafter referred to as *input map*. The fusion of the measurement drive with the input map yields the *updated map* that serves as input map for the next measurement drive. When no initialization is available, the first measurement drive is considered as input map for the subsequent measurement drive.

In single-drive processing, the recorded measurement drive is preprocessed to extract lane markings and combine these with vehicle motion data and GNSS measurements. Specifically, the base line is identified, as prerequisite for the lateral correction. In this work, the base line is defined as a uniquely identifiable marking sequence, e.g. the right-most thin lane marking. The base line correction then fuses the globally referenced base lines by computing an updated base line. In

---

[1]The curve minimal radii on high-velocity roads are typically conditioned to be larger than 200 m.
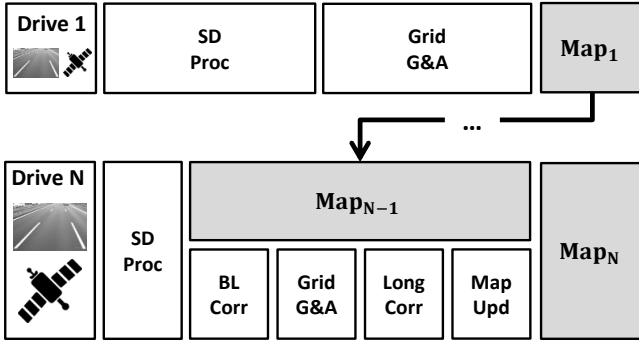
Fig. 3. **High-Level Overview of the Map Generation Framework.** Each measurement drive is fused separately with the map yielding an updated map. The first drive is taken as input map for the succeeding measurement drive. The individual steps are abbreviated: Single-Drive Processing (SD Proc), Base Line Correction (BL Corr), Grid Generation and Analysis (Grid G&A), Longitudinal Correction (Long Corr) and Map Update (Map Upd).
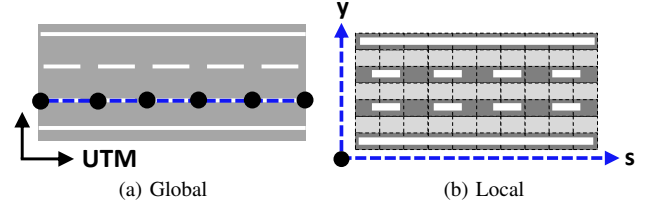

Fig. 4. **Map Representation.** The global part contains the base line that is stored as a polygonal chain referenced in the global coordinate system, while the local part represents lane marking information in a fine-grained grid indexed by the arc length of the global polygonal chain. The light gray grid cells represent intermediate cells, while grid cells in dark gray represent regular cells.

the succeeding step, the grid is generated and analyzed by extracting significant, unique lane marking changes. These lane marking changes then serve as input to the longitudinal correction that adjusts and refines the grids such that, as a result, the input map and the processed drive data match with regard to the base line and the lane marking changes. Finally, the grids of the input map and of the measurement drive are fused to yield an updated grid. The updated grid and the updated base line are stored as updated map.

A. Map Representation

The map is split into two parts, a *global* and a *local* part. The global part describes the course of the roads in global coordinates and is stored as a polygonal chain of two-dimensional way points $\mathbf{p_i}$ with their respective uncertainties $\mathbf{\Sigma_i}$ (Figure 4a). The local part, in contrast, describes road information, specifically lane markings, and is arranged in a fine-grained grid G_s along the base line at position s having C grid cells (Figure 4b). Each cell thereby stores lane marking items for solid, dashed and transition lane markings. The purpose of the latter is to represent lane openings and closures. Generally, items are indexed by grid coordinates $\mathbf{n} = (s, y)$ describing the position s of the cell along the base line and the lateral perpendicular distance y. This representation allows a separate update of highly accurate local information in the grid and the global position information in the base line.

Note, besides the base line and the fused grid, the map also stores the grids of all measurement drives to allow retroactive reasoning about the existence of lane markings.

B. Single Drive Processing

The intention of the single-drive processing is to extract relevant information from each drive individually as a preparation for the subsequent steps. It is subdivided into lane marking extraction, vehicle pose computation and lane marking analysis.

The details of the lane marking extraction algorithm are out of the scope of this paper. In short, we employed an algorithm that searches for dark-light-dark patterns with fixed widths according to the lane marking norms [14]. Detected regions in the images are grouped into lane marking clusters that are transformed into top-view and therein processed to compute the lane marking centerline. The centerline is stored as a polygonal chain.

Next, the position information from the GNSS receiver is corrected by vehicle motion data. The latter is computed by a novel visual odometry algorithm tuned for standardized roads, that is presented in-depth in section IV. The computed vehicle motion data is fused with GNSS measurements as introduced in our previous work [9] using a graph-based notation and non-linear least square optimization. The obtained, globally referenced vehicle poses are then used to transform extracted lane markings into the global reference system.

Finally, the lane marking information is analyzed to identify the base line and the marking change points, e.g. a transition from solid to dashed. Obviously, the selection and detection of the base line are crucial for the success of the algorithm since it serves as core association data across measurement drives. The base line in this paper is chosen as the right-most thin lane marking, but it may be chosen arbitrarily.

After the marking change identification, the marking change points are checked for plausibility with the respective marking change points of the input map by comparing their positions. If they do not lie within the assumed GNSS uncertainty range, the drive is considered implausible.

C. Base Line Correction

Given the uncertainty of global vehicle positions, the base lines of the measurement drive and the input map are expected to deviate in the global reference system as indicated in figure 5. Hence, the purpose of this step is to correct the base lines laterally such that the base lines coincide afterwards. To accomplish this, a new base line is computed by fusing the way points of the base lines.

The base line of the input map B^M and the measurement drive B^D are each represented by a polygonal chain of two-dimensional points $\mathbf{p_i}$ with their respective uncertainties $\mathbf{\Sigma_i}$. Given a way point on the base line of the input map $\mathbf{p_i^M}$ with uncertainty $\mathbf{\Sigma_i^M}$ and its perpendicular projection onto the base line of the measurement drive $\mathbf{\tilde{p}_j^D}$ with its propagated
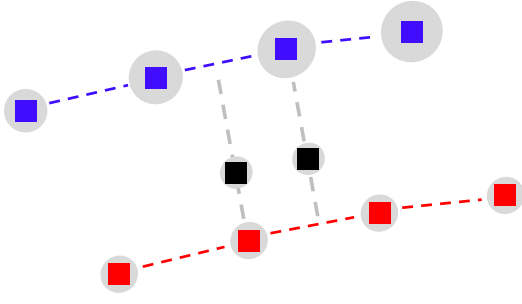
Fig. 5. **Base Line Correction.** The base line of the measurement drive is shown in blue, the base line of the input map in red. The covariance ellipses are visualized in gray. The corrected base line is displayed for two way points in black. The projection onto the base line of the measurement drive is perpendicular to base line of the input map and vice versa.

uncertainty $\tilde{\mathbf{\Sigma}}_{\mathbf{j}}^{\mathbf{D}}$ [15], the updated position is computed by a weighted average in equation (1), while the new uncertainty is computed in equation (2).

$$\hat{\mathbf{p}}_{\mathbf{k}}^{\mathbf{F}} = \mathbf{p}_{\mathbf{i}}^{\mathbf{M}} + \mathbf{\Sigma}_{\mathbf{i}}^{\mathbf{M}}(\mathbf{\Sigma}_{\mathbf{i}}^{\mathbf{M}} + \tilde{\mathbf{\Sigma}}_{\mathbf{j}}^{\mathbf{D}})^{-1}(\tilde{\mathbf{p}}_{\mathbf{j}}^{\mathbf{D}} - \mathbf{p}_{\mathbf{i}}^{\mathbf{M}}) \qquad (1)$$

$$\mathbf{\Sigma}_{\mathbf{k}}^{\mathbf{F}} = \tilde{\mathbf{\Sigma}}_{\mathbf{j}}^{\mathbf{D}}(\mathbf{\Sigma}_{\mathbf{i}}^{\mathbf{M}} + \tilde{\mathbf{\Sigma}}_{\mathbf{j}}^{\mathbf{D}})^{-1}\mathbf{\Sigma}_{\mathbf{i}}^{\mathbf{M}} \qquad (2)$$

This computation is performed for all way points on both base lines as indicated in figure 5 yielding a refined, more accurate updated base line. Given the new way points, the base lines of the measurement drive and the input map coincide with the exception of the respective time stamps which are not modified by this correction. Note, the base line is only corrected laterally which is sufficient considering the limited curvatures of high-velocity roads.

D. Grid Generation and Analysis

After the position correction of the base line, the grid is generated and filled with the extracted lane marking information (Figure 4b). To generate the grid, imaginary vertical lines perpendicular to the base line are created in equal distances. Then, cells are created along these lines in predefined distances according to the regulations for lane widths. While these cells are supposed to contain regular lane marking information, intermediate cells are defined in between (see Figure 4b) that contain the transition of solid lines from one lane boundary to another, e.g. when a lane begins or ends.

The extracted and transformed lane marking centerlines are next distributed to the grid cells. Thereby, it is distinguished between solid and transition lane markings and dashed lane markings. Dashed lane markings are distinguished from solid and transition lane markings by thresholding the length of the lane marking centerline.

For solid and transition lane markings, each cell that is occupied by a centerline point is added a four-tuple $(s, y, \phi, \mathbf{\Sigma})$ describing the position s, lateral distance y, orientation ϕ and their respective uncertainty $\mathbf{\Sigma}$. Dashed lane markings are not stored point-wise but are described as one lane marking item by a five-tuple $(s_{\text{start}}, s_{\text{end}}, y_{\text{mean}}, \phi_{\text{mean}}, \mathbf{\Sigma})$. The item includes the start and end positions s_{start} and s_{end} as

well as the average lateral distance y_{mean}, orientation ϕ_{mean} and the respective uncertainty $\mathbf{\Sigma}$.

After the generation of the grid, it is analyzed to identify lane marking changes in grid-relative coordinates.

E. Longitudinal Correction

The input to the longitudinal correction are the grids of the measurement drive and the input map. The purpose of this step is to align the grids of the measurement drive and the input map in longitudinal direction by comparing associated lane marking changes. The association of lane marking changes is performed by looking for equal lane marking changes, e.g. solid to dashed, in a search window according to the assumed GNSS uncertainty. The longitudinal
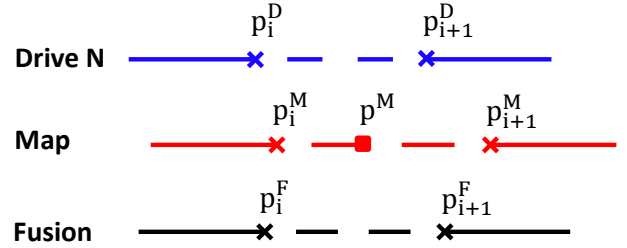

Fig. 6. **Longitudinal Correction.** The lane marking data contained in the grids is shifted and scaled incorporating the uncertainties of the available data.

correction involves both, a global position and a grid update, meaning that the lane markings are shifted and rescaled along the base line. Similar to the base line correction, a lane marking change $LC_i = (p_i, \sigma_i)$ is a point feature described by a one-dimensional position p_i along the base line and its uncertainty σ_i^2. Given two neighboring lane marking changes in the measurement drive LC_i^D and LC_{i+1}^D and associated lane marking changes in the input map LC_i^M and LC_{i+1}^M, updated positions and uncertainties are computed according to equation (1) and (2) yielding LC_i^F and LC_{i+1}^F as shown in figure 6. With these corrected marking change points, the lane markings in between are rescaled accordingly for the measurement drive grid and all single-drive grids stored in the input map.

For example, in figure 6, given the fused positions p_i^F and p_{i+1}^F and the positions of the input map p_i^M and p_{i+1}^M, a position p^M in the interval $[p_i^M, p_{i+1}^M]$ is rescaled by equation (3) yielding the rescaled position p_{upd}^M.

$$p_{\text{upd}}^M = p^M + \Delta p_i + (\Delta p_{i+1} - \Delta p_i)\frac{p^M - p_i^M}{p_{i+1}^M - p_i^M} \qquad (3)$$

with $\Delta p_i = p_i^F - p_i^M$ and $\Delta p_{i+1} = p_{i+1}^F - p_{i+1}^M$.

After aligning the grids longitudinally, all single-drive grids coincide with regard to the lane marking changes.

F. Map Update

In the final map update, the fused grid is computed from all single-drive grids and stored persistently as new grid alongside the updated base line.
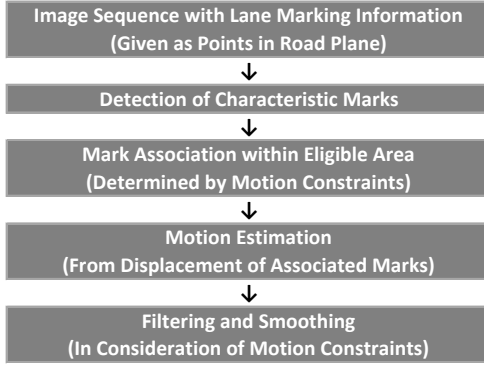
Fig. 7. **High-Level Overview of LMBVO.**

Fig. 8. **Lane Marking Based Visual Odometry.**

The grid fusion for solid and dashed lane markings is finally performed by averaging the lane marking items contained in the grid cells. For solid lane markings, the averaging is done cell-wise, while the averaging is performed dash-wise for dashed lane markings.

IV. LANE MARKING BASED VISUAL ODOMETRY

As outlined in Section III-B, one fundamental processing step is the fusion of GNSS measurements and vehicle motion data to improve the vehicle's position data. Since the sensor system is equipped solely with a GNSS receiver and a monocular camera, visual odometry is chosen to estimate the motion of the vehicle.

A problem that is inherent to monoscopic visual odometry in general, and to low-structured, high-velocity environments in particular is the estimation of the scale.

Recent approaches therefore estimate the scale via the calibrated ground plane in the close vicinity of the vehicle [16] or by additionally using computed vanishing points [17]. The latter approach hardly works on high-velocity roads, because mostly one vanishing point is extractable reliably, while the former approach requires features on the road in the close surrounding of the vehicle for robust scale estimations. Unfortunately, these features are rarely available due to the higher motion blur on high-velocity roads.

To compensate for the mentioned weaknesses, we propose a new visual odometry algorithm, Lane Marking Based Visual Odometry (LMBVO), that exploits the regulations of the road construction and lane markings. Figure 7 summarizes the individual steps of the new visual odometry algorithm.

The input to the visual odometry algorithm are lists of extracted lane marking centerlines transformed into topview at succeeding time steps t and $t + 1$. The idea of the new algorithm is to estimate the motion of the vehicle by tracking lane marking centerlines from frame-to-frame and to compute the relative motion in the topview vehicle coordinate system as shown in figure 8.

The position determination of the marks relative to the camera is critical to this approach. This is not feasible for solid lines having no dedicated start and end, so that solid lines are excluded. Therefore, only dashed marks are kept
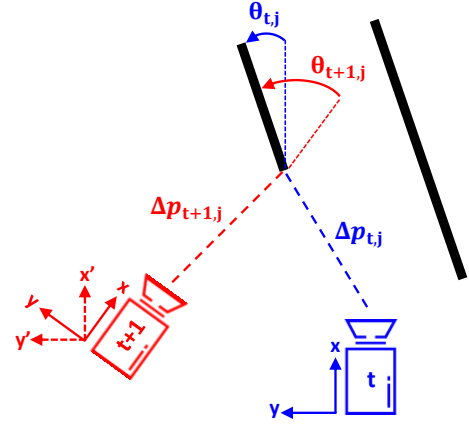
for further processing, because they typically have a fixed length on high-velocity roads. Hereafter, the start positions $\mathbf{s_i}$ and the orientations ϕ_i of eligible dashed marks are used to estimate the two-dimensional motion of the vehicle.

A. Application Area

To uniquely associate dashed marks from frame-to-frame, multiple conditions regarding camera setup and vehicle dynamics have to be met. The camera capture frequency is denoted as f. The maximal velocity of the vehicle is v^{max}, while the maximal orientation deviation of the vehicle from the road is ϕ^{max}.

Regarding road regulations, the fixed length of a dashed mark is l_{dashed}, while the minimal gap length is $l_{\mathrm{gap}}^{\mathrm{min}}$. The minimal lane width is given by w^{min}.

Then, the maximum longitudinal distance between two camera frames is $d_{\mathrm{lon}}^{\mathrm{max}} = \frac{v^{\mathrm{max}}}{f}$ such that dashed marks are uniquely associated if $d_{\mathrm{lon}}^{\mathrm{max}} < l_{\mathrm{dashed}} + l_{\mathrm{gap}}^{\mathrm{min}}$ holds.

Likewise, the maximum lateral distance is given by $d_{\mathrm{lat}}^{\mathrm{max}} = \sin(\phi^{\mathrm{max}}) \cdot d_{\mathrm{lon}}^{\mathrm{max}}$. So, to not accidently associate dashed marks with neighboring marks, $d_{\mathrm{lat}}^{\mathrm{max}} < w^{\mathrm{min}}$ must hold.

B. Processing

For all consecutive images, any eligible dashed mark that exists in image t is searched for in the succeeding image $t + 1$. The search area is restricted to an area around the position in the first image, given the assumptions in section IV-A. Given two eligible lane marking clusters representing the same dashed mark j, the motion estimation is computed as follows. The start positions and orientations relative to the camera are given by $(\Delta\mathbf{p}_{t,j}, \phi_{t,j})$ and $(\Delta\mathbf{p}_{t+1,j}, \phi_{t+1,j})$ as shown in figure 8.

The base coordinate system CS_t for the computation is the one from time step t. The change in orientation $\Delta\phi$ is independent of the coordinate system and defined by:

$$\Delta\phi_{t \to t+1,j} = \Delta\phi_{t,j} - \Delta\phi_{t+1,j} \qquad (4)$$

To simplify the computation of the translation, an additional coordinate system at time step $t + 1$, CS'_{t+1}, is defined (dashed axes in figure 8) that is axis aligned to the coordinate

system CS_t. The rotation from CS_{t+1} to CS'_{t+1} is computed by:

$$\mathbf{R}_{CS_{t+1}\to CS'_{t+1},j} = \begin{pmatrix} \cos\Delta\phi & -\sin\Delta\phi \\ \sin\Delta\phi & \cos\Delta\phi \end{pmatrix} \quad (5)$$

with $\Delta\phi = -\Delta\phi_{t\to t+1,j}$. Finally, the translation with respect to CS_t is computed by:

$$\Delta\mathbf{p}_{t\to t+1,j} = \Delta\mathbf{p}_{t,j} - \mathbf{R}_{CS_{t+1}\to CS'_{t+1},j} \cdot \Delta\mathbf{p}_{t+1,j} \quad (6)$$

C. Post-Processing

In a post-processing step, the movement is averaged over all detected dashed marks in the frame-to-frame comparison. Since dashed marks are not visible in all images, the vehicle motion cannot be computed for every time step. To nevertheless close the gaps, the missing motions are interpolated and afterwards smoothed by past and future motion estimations, as the vehicle dynamics are restricted.

V. EVALUATION

For evaluation purpose, high-cost and high-precision sensor data is recorded and taken as the ground-truth reference. In addition, available construction norms for highways and painted lane markings are used as a further reference for quantitative evaluation. The former specifies the lane widths to be either $3.5\,\mathrm{m}$ or $3.75\,\mathrm{m}$, while the latter regulates the length of dashed lane markings to be $6\,\mathrm{m}$ with the gap lengths being either $3\,\mathrm{m}$, $6\,\mathrm{m}$ or $12\,\mathrm{m}$.

The evaluation is split into two parts. The first part evaluates the results of the proposed visual odometry algorithm, while the second part analyzes the quality of the generated map.

A. Evaluation Setup

The test track is a German highway close to Karlsruhe with renewed lane markings on a fresh ground. The total length of the test track is approximately $2.8\,\mathrm{km}$ consisting of three lanes on the main carriageway as well as entry and exit lanes. The measurement vehicle is an Audi Q7 with a monocular gray-scale camera (PointGrey Flea3, 2.8Mpx, 15Hz) mounted to the roof-top, a low-cost GNSS receiver (u-blox M8T, 1Hz) and a high-cost RTK-DGPS system (OxTS RT3003, 100Hz). Three measurement drives were taken with the weather being partly cloudy and excellent view.

B. Lane Marking Based Visual Odometry (LMBVO)

To evaluate the presented visual odometry algorithm, the computed vehicle motion is compared to the planar vehicle motion of the high-cost DGPS-RTK device accumulated in a common reference system.

	Drive 1	Drive 2	Drive 3
Δs [m]	8.89	15.73	-1.88
Δs [%]	0.30	0.50	0.06
$\Delta\phi_n$ [°]	-5.64	-11.49	1.57
$\Delta\phi_{0\to n}$ [°]	1.43	-7.96	0.80

TABLE I

COMPARISON OF ACCUMULATED LMBVO AND OXTS DGPS.

Quantitative results are summarized in Table I for 1500 images on the test track. The table compares the absolute and relative, accumulated driven distance Δs as well as the difference in the final orientation angle $\Delta\phi_n$ and the angular difference between the start and end point $\Delta\phi_{0\to n}$. Looking at the results, the distance from the start to the end point, taken as a measure for the accuracy in the direction of travel, only differs by $\Delta s < 1\%$. The difference in the final orientation, $\Delta\phi_n = \phi_{\mathrm{LMBVO},n} - \phi_{\mathrm{GPS},n}$, as well as the difference of the angles from the start to the end point, $\Delta\phi_{0\to n} = \phi_{\mathrm{LMBVO},0\to n} - \phi_{\mathrm{GPS},0\to n}$, are acceptably small.

	mean	median	stddev
e_{lon} [m]	0.006 61	0.008 71	0.036 50
e_{lat} [m]	0.006 45	0.008 38	0.012 20
e_ϕ [°]	$-0.003\,25$	$-0.005\,18$	0.036 30

TABLE II

COMPARISON OF LMBVO TO GROUND TRUTH DATA

Table II lists the statistical errors for the motion estimation. Therefore, the lateral, longitudinal and orientation motion from one image frame to another is compared to the respective motion of the ground truth yielding the signed errors in the table. The relative longitudinal error is in the sub-percentage range with a mean relative error of 0.36%. On high-velocity roads, the lateral movement and the orientation change are expected to be of small scale such that the relative error for both is mostly affected by measurement noise. Figure 9 exemplarily shows the error development for the orientation over all recorded images. The plot shows that the LMBVO algorithm follows the small-scale orientation change of the ground truth measurements.
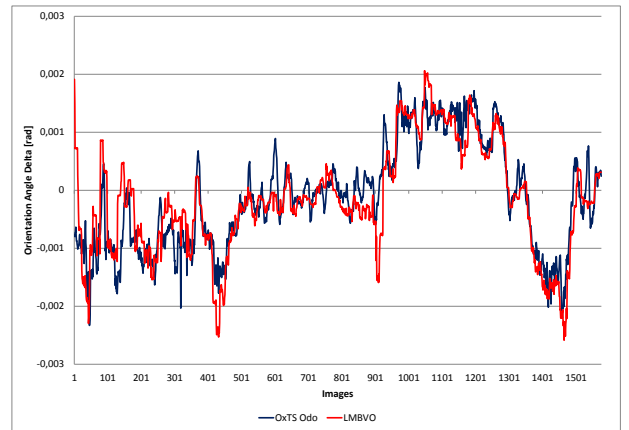

Fig. 9. **Evaluation of the Orientation Angle Differences.**

In summary, the evaluation of LMBVO shows that promising results have been achieved with a trivial approach to estimate the vehicle motion in high-velocity scenarios on standardized roads.

C. Evaluation of Map Generation

The evaluation of the map generation framework is three-fold using the following approaches for comparison:

Fig. 10. **Visual Comparison of Generated Map and Aerial Imagery**.

Fig. 11. **Quantitative Comparison to DGPS-RTK Data.** Lateral offset of the generated map base line against the base line of a map generated with RTK-DGPS position information.

- Qualitative, visual comparison to aerial images
- Quantitative comparison to RTK-DGPS measurements
- Quantitative comparison to construction norms

Qualitative Evaluation

The qualitative comparison is based on satellite images from MapBox[2]. The visual comparison reveals that the number of dashes on the main carriageway in the aerial image equals the number of dashes detected by the algorithm. The road course in the aerial images complies with the detected road course. A sample road section is visualized in figure 10 with the computed map overlayed on top of the aerial image.

Quantitative Comparison to RTK-DPGS

The quantitative comparison of the generated map to the high-cost position data is performed to evaluate the global position accuracy. Thereby, the lateral deviation is computed by comparing both base lines, while the longitudinal deviation is checked by comparing the characteristic marking changes. Figure 11 plots the lateral deviation of both base lines over the track length.

	Δ[m]	Δ_{lon}[m]	Δ_{lat}[m]
Marking Change 1	8.41	8.45	0.33
Marking Change 2	8.41	8.37	-0.85
Marking Change 3	7.67	7.64	-0.78
Marking Change 4	7.20	7.20	-0.31
Marking Change 5	6.47	6.47	-0.09

TABLE III

QUANTITATIVE COMPARISON TO DGPS-RTK DATA.

The longitudinal deviation for five marking changes in a single drive is listed in Table III. The first value is the
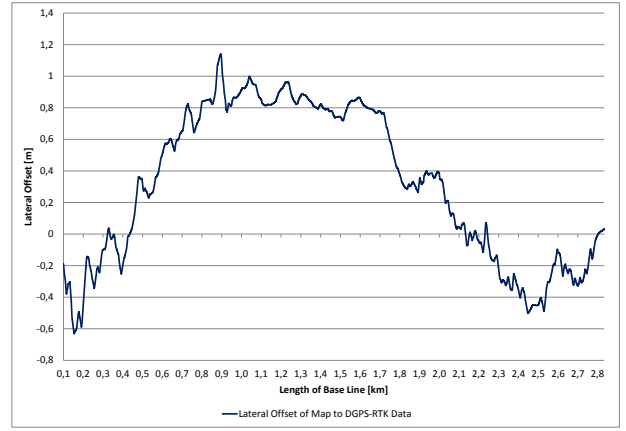
Euclidean distance, followed by the distance along the base line Δ_{lon} and the distance normal to the base line Δ_{lat}. As the base line is not necessarily straight, Δ_{lon} may be larger than the euclidean distance.

The constant offset of around $8\,\text{m}$ shows the constancy of the local grid of low-cost and high-cost map, but it also reveals weaknesses in the global position accuracy. However, the longitudinal offset has been visible in all measurement drives such that this error might be caused by a constant GPS error or by time sychronization issues.

Quantitative Comparison to Construction Norms

To reason about the local accuracy of the generated map, the grid information, i.e. the extracted lane markings, are compared to the construction norms for German highways [18] and the painting of lane markings [19]. Of particular interest are the lane widths as well as the defined lengths for dashes and gaps. To accurately represent the lane marking information in the grid, grid cells are created along the base in equal distances of $10\,\text{cm}$.

The lane widths of the generated map are listed in Table IV. The exact width of a lane is not known for every German road, because it depends on the traffic emergence which is not apparent to us. The results show an overall consistency with the referenced norm.

		mean	median	stddev	RAA
Map	Lane 1 [m]	3.78	3.78	0.09	3.5 / 3.75
	Lane 2 [m]	3.84	3.83	0.04	3.5 / 3.75
	Lane 3 [m]	3.82	3.82	0.07	3.5 / 3.75
OxTS	Lane 1 [m]	3.77	3.76	0.12	3.5 / 3.75
	Lane 2 [m]	3.83	3.83	0.05	3.5 / 3.75
	Lane 3 [m]	3.83	3.81	0.13	3.5 / 3.75

TABLE IV

QUANTITATIVE COMPARISON OF LANE WIDTHS.

The extracted lane markings are compared in Table V. The

[2]http://www.mapbox.com/

results again show an overall consistency with the reference norm which is apparent in the single-drive grids like in the final map. As the dash length mean value is close to the respective median and the standard deviation is in the lower decimeter range, an accurate dash representation can be assumed. The mean length deviates about 1% from the norm.

		mean	median	stddev	RMS
Map	Dash [m]	6.06	6.07	0.12	6
	Small Gap [m]	5.83	5.87	0.28	6
	Large Gap [m]	11.80	11.80	0.48	12
OxTS	Dash [m]	6.06	6.07	0.13	6
	Small Gap [m]	5.89	5.88	0.18	6
	Large Gap [m]	11.80	11.80	0.37	12

TABLE V

QUANTITATIVE COMPARISON OF LANE MARKINGS.

Concerning the gap lengths of both, small and long gaps, the average deviation and the standard deviation are larger, but still consistent to the norm in the meaning of not deviating more than 5%. Both comparisons show that the multi-drive map generation framework is capable to represent the lane marking information with an adequate and desired accuracy.

VI. CONCLUSION

In this paper we presented an algorithmic framework for the automated generation of digital road maps for low-structured, but standardized high-velocity road environments, like highways, using low-cost sensor data. The map representation and the generation process are thereby split into a global and local part. The global part captures the course of the road's carriageway, while the local part contains lane marking information.

One of the core components of the map generation framework has been a novel visual odometry algorithm that exhibits standardized construction norms to estimate the scale of the vehicle motion. Despite the triviality of the approach, the results have been promising for future research. The accuracy in the long term accumulated steps enables its use for short term localization applications in areas where global position information is poor or not available, such as tunnels.

The results of the generated map show a high local accuracy conforming to the reference construction norms, while the global accuracy is in the meter range which is adequately acceptable, at least for high-velocity scenarios.

In future work, variations on the presented techniques will be elaborated, for example to perform a combined base line and grid update which becomes important for highway intersection areas wherein the assumed road geometry is violated. Finally, we plan to incorporate additional road features like traffic signs.

Currently, the map is constructed in two dimensions only but we plan to further enhance the presented framework to output a three dimensional map. Therefore, to obtain three-dimensional vehicle positions, we will fuse three-dimensional visual odometry data with GNSS measurements incorporating the scale from GNSS Doppler (velocity) and LMBVO measurements.

To conclude, the presented algorithm shows that the automated digital road map generation with low-cost sensor data is achievable, providing highly accurate local data for vision-based vehicle localizations on standardized, high-velocity roads.

REFERENCES

[1] W. Burgard, O. Brock, and C. Stachniss, *Map-Based Precision Vehicle Localization in Urban Environments*. MIT Press, 2008.

[2] J. Ziegler et. al., "Making Bertha Drive – An Autonomous Journey on a Historic Route," *IEEE Intelligent Transportation Systems Magazine*, vol. 6, no. 2, pp. 8–20, 2014.

[3] IVI Vehicle Enabling Research Program funded by U.S. Departement of Transportation, "Enhanced Digital Maps," 2004.

[4] U. Noyer, J. Schomerus, H. Mosebach, J. Gacnik, C. Loper, and K. Lemmer, "Generating High Precision Maps for Advanced Guidance Support," in *IEEE Intelligent Vehicles Symposium (IV)*, June 2008, pp. 871–876.

[5] S. Rauch, A. Savkin, T. Schaller, and P. Hecket, "Hochgenaue Fahrzeuglokalisierung und kollektives Erlernen hochgenauer digitaler Karten," *Automatisierungssysteme, Assistenzsysteme und eingebettete Systeme für Transportmittel*, 2012, Language: German.

[6] H. Deusch, D. Nuss, P. Konrad, M. Konrad, M. Fritzsche, and K. Dietmayer, "Improving Localization in Digital Maps with Grid Maps," in *IEEE International Conference on Intelligent Transportation Systems*, October 2013, pp. 1522–1527.

[7] A. Wimmer, T. Jungel, M. Glück, and K. Dietmayer, "Automatic Generation of a Highly Accurate Map for Driver Assistance Systems in Road Construction Sites," in *IEEE Intelligent Vehicles Symposium*, June 2010, pp. 281–286.

[8] C. Guo, J. i. Meguro, Y. Kojima, and T. Naito, "Automatic lane-level map generation for advanced driver assistance systems using low-cost sensors," in *2014 IEEE International Conference on Robotics and Automation (ICRA)*, May 2014, pp. 3975–3982.

[9] M. Schreiber, A. M. Hellmund, and C. Stiller, "Multi-Drive Feature Association for Automated Map Generation Using Low-Cost Sensor Data," in *2015 IEEE Intelligent Vehicles Symposium (IV)*, June 2015, pp. 1140–1147.

[10] O. Pink and C. Stiller, "Automated Map Generation from Aerial Images for Precise Vehicle Localization," in *IEEE Conference on Intelligent Transportation Systems*, September 2010, pp. 1517–1522.

[11] D. Betaille and R. Toledo-Moreo, "Creating Enhanced Maps for Lane-Level Vehicle Navigation," *IEEE Transactions on Intelligent Transportation Systems*, vol. 11, no. 4, pp. 786–798, December 2010.

[12] S. Schroedl, K. Wagstaff, S. Rogers, P. Langley, and C. Wilson, "Mining GPS Traces for Map Refinement," *Data Mining and Knowledge Discovery*, vol. 9, no. 1, pp. 59–87, July 2004.

[13] A. Noureldin, T. B. Karamat, and J. Georgy, *Fundamentals of inertial nav- igation, satellite-based positioning and their integratio.* Springer Berlin, 2010.

[14] T. Veit, J. P. Tarel, P. Nicolle, and P. Charbonnier, "Evaluation of Road Marking Feature Extraction," in *2008 11th International IEEE Conference on Intelligent Transportation Systems*, Oct 2008, pp. 174–181.

[15] S. Schlegel, N. Korn, and G. Scheuermann, "On the Interpolation of Data with Normally Distributed Uncertainty for Visualization," *IEEE Transactions on Visualization and Computer Graphics*, vol. 18, no. 12, pp. 2305–2314, Dec 2012.

[16] A. Geiger, J. Ziegler, and C. Stiller, "Stereoscan: Dense 3d reconstruction in real-time," in *Intelligent Vehicles Symposium (IV)*, 2011.

[17] J. Gräter, T. Schwarze, and M. Lauer, "Robust scale estimation for monocular visual odometry using structure from motion and vanishing points," in *2015 IEEE Intelligent Vehicles Symposium (IV)*, June 2015, pp. 475–480.

[18] Forschungsgesellschaft für Straßen- und Verkehrswesen, "Richtlinien für die Anlage von Autobahnen," 2008.

[19] ——, "Richtlinien für die Markierung von Straßen (RMS-2)," 1980.